INFLUENCE OF SCALE ON THE PENETRATION OF TUNGSTEN RODS INTO STEEL-BACKED ALUMINA TARGETS

P. LUNDBERG, L. WESTERLING and B. LUNDBERG

National Defence Research Establishment, FOA, S-172 90 Stockholm, Sweden

Summary — As ballistic tests are often performed in reduced geometrical scale, the scaling laws are important for the interpretation of the results. In this study, we tested the validity of replica scaling, by which we mean that all geometrical dimensions are scaled uniformly, while the materials and the impact velocity are kept the same. Long tungsten projectiles with length-to-diameter ratio 15 were fired against unconfined alumina targets with steel backing. The tests were carried out with impact velocities 1500 m s^{-1} and 2500 m s^{-1}, and in three different scales with projectile lengths 30, 75 and 150 mm (diameters 2, 5 and 10 mm). The alumina targets were photographed by means of a high-speed camera, and the tungsten projectiles were photographed inside the alumina targets by means of flash radiography. Also, the residual penetrations in the steel backings were measured. The Johnson–Holmquist model for ceramic materials was implemented into the AUTODYN code, which was used for simulation of the experiments. The agreement between results of experiment and simulation was fair, and over the tested interval of scales replica scaling was found to be valid with reasonable accuracy.

Key words: replica, scale, impact, penetration, rod, projectile, ceramic, target.

NOTATION

A, B, C, m, n, T_m, T_0	constitutive parameters (Johnson–Cook)
C_r	specific heat
D	diameter
E	Young's modulus
G	shear modulus
H	hardening modulus
K_{1c}	fracture toughness
L	length
$\mathbf{P}$	parameter vector
P	penetration
t	time
T	temperature
v	impact velocity
ε^p	plastic strain
$\dot{\varepsilon}^p$	plastic strain rate
$\dot{\varepsilon}_0$	strain rate threshold
λ	length scale factor (model to prototype)
σ	yield limit
ρ	density

Subscripts

b	steel backing
f	final
i	initial
p	tungsten projectile
t	alumina target

Superscript

*	reference quantity

INTRODUCTION

Penetration of tungsten projectiles with large length-to-diameter ratio into targets of various materials (e.g. steel, ceramics) has been studied extensively. Reference [1] gives, among other

things, a general description of the penetration process in semi-infinite steel targets and a summary of experimental results (e.g. influence of impact velocity, target hardness etc.). The mechanisms involved when a projectile penetrates a thick ceramic target (steel-encased) are described by Shockey *et al.* [2].

Most of the penetration experiments are performed in reduced scale in order to simplify handling and decrease costs. Scaling laws are therefore essential for translation of results from tests to full scale. Usually, replica scaling is used, by which we mean that the geometrical dimensions are scaled uniformly, while the materials and the impact velocity are kept the same. There may be several reasons for lack of scaling which are of a practical nature. One may be that some geometrical details in full scale are not properly considered. Another may be that the material properties are size-dependent due to the manufacturing process. A more fundamental reason may be that some dimensionless parameters (pi terms) containing material properties, such as fracture toughness and strain rate sensitivity, do not remain constant in replica scaling.

The validity of replica scaling in penetration mechanics has been subjected to several studies. For example Magness and Leonard [3] reported improved projectile performance with increased scale when depleted uranium and tungsten projectiles penetrate different steel targets. On the other hand, Holmberg *et al.* [4] studied replica scaling for tungsten projectiles which penetrate oblique steel plates and found no influence of scale.

In this paper we are concerned with the penetration of long rod projectiles into ceramic targets. We have chosen to study the validity of replica scaling for a simple target geometry which allows proper scaling of all geometrical dimensions. Thus, the targets were unconfined alumina cylinders with cylindrical steel backings, and the tests were carried out in three different scales for two impact velocities.

For simulation of the tests, we implemented the Johnson–Holmquist constitutive model [5] into the AUTODYN code and treated the alumina as strain-rate independent. Therefore effects of strain-rate were not simulated, as they were in [6].

EXPERIMENTS

The impact tests were carried out by firing flat-ended cylindrical tungsten projectiles with lengths 30, 75 and 150 mm and length-to-diameter ratio 15 (diameters 2, 5 and 10 mm) at $1500 \, \text{m s}^{-1}$ and $2500 \, \text{m s}^{-1}$ into replica-scaled targets. The projectiles were launched with a two-stage light-gas gun. They were accelerated using a pushing sabot (with a pusher plate made of titanium), except in the 150 mm projectile tests at $2500 \, \text{m s}^{-1}$, where a pulling sabot was used. In the latter case, three quarters of the projectile length was threaded (M10 × 1). The sabot was separated aerodynamically from the projectile, and the pieces were caught by a trap consisting of a vertical armour plate with a central hole. For the experiments at $2500 \, \text{m s}^{-1}$ with a pushing sabot, two armour plates were needed to catch the pusher plate. The target set-ups were free and lying on a V-profile about three meters from the muzzle of the gun. Each target set-up consisted of an alumina cylinder (referred to as target), glued with Araldite D (Ciba Geigy) on a steel cylinder (referred to as backing), both with circular cross-sections. The length of the alumina target was chosen so that at least one third of the total penetration would occur in the steel backing. The designs of the targets, backings and projectiles are shown in Fig. 1.

The projectiles were made from a sintered tungsten alloy (DX 2 HCMF from Pechiney). The alumina targets (99.7% Al_2O_3-powder from Vereinigte Aluminiumwerke) were produced by Ifö Ceramics by CIP-processing (density $3809 \, \text{kg m}^{-3}$ with standard deviation $16 \, \text{kg m}^{-3}$, sound speed $10.02 \, \text{km s}^{-1}$ with standard deviation $0.14 \, \text{km s}^{-1}$). The backing material was a steel for hardening and tempering (SIS 2541-03) with a Vickers hardness of 317 HV 0.1 (standard deviation 15 HV 0.1). Photographs of the alumina targets and tungsten projectiles for the $1500 \, \text{m s}^{-1}$ experiments are shown in Fig. 2.

Three 150 kV X-ray flashes in front of the sabot catcher plates were used to determine the velocity and the orientation of the tungsten projectile (two from above and one from the side). The angle of attack at impact was estimated by linear extrapolation.
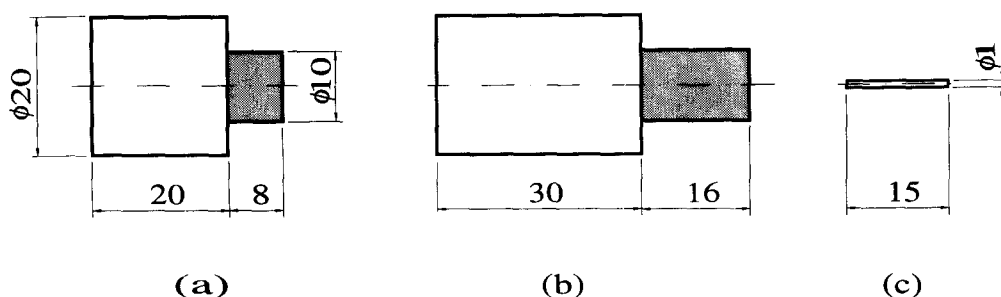
Fig. 1. Steel backing and alumina target (shaded) for (a) 1500 m s^{-1} and (b) 2500 m s^{-1}. (c) Tungsten projectile. Dimensions are given in terms of the projectile diameter.
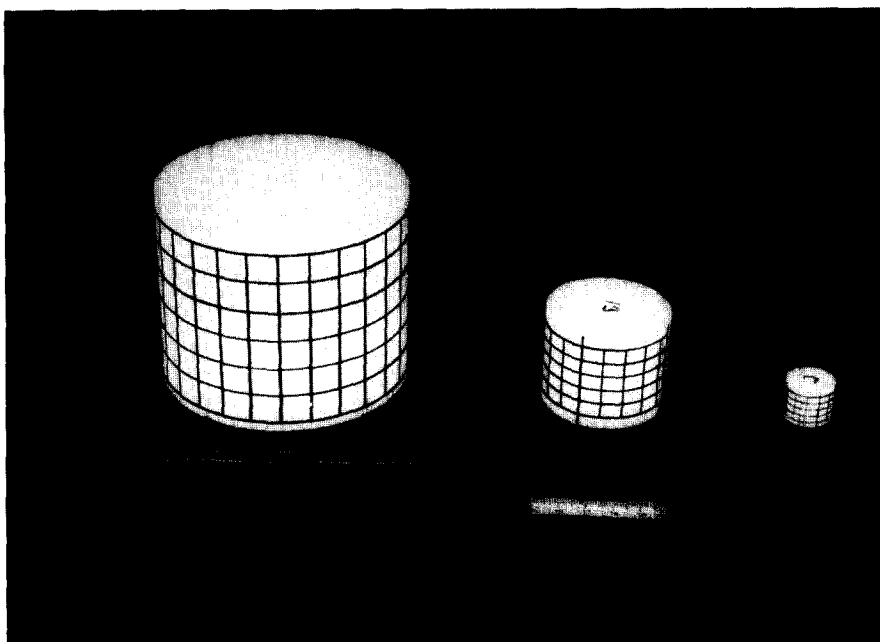

Fig. 2. Alumina targets and tungsten projectiles for 1500 m s^{-1} tests.

In all tests at 1500 m s^{-1}, and for the 75 mm length projectiles at 2500 m s^{-1}, the position of the projectile tip during penetration was determined from shadowgraphs obtained using flash radiography. A 1.2 MV X-ray flash was used except in the smallest-scale tests, where a 150 kV X-ray flash was used. The exposures were made when the projectile had penetrated approximately half the length of the alumina target.

An Imacon 790 high-speed camera and a measuring microscope were generally used in order to determine the expansion of the front end of the alumina target during the penetration process. A square grid was painted on the target and a paper sheet with parallel vertical lines was used as a background reference, as shown in Fig. 3. Eight pictures (Kodak Tri-X film) were taken with 4.88 μs interval and 1 μs exposure time. Illumination was provided by an Imacon 20/50 xenon flash. Triggering of the X-ray flashes, the Imacon camera and the xenon flash was achieved with a pulse from a copper grid mounted on the front of the alumina target.

In one case (150 mm projectile at 2500 m s^{-1}), two 150 kV X-ray pictures were used instead of the Imacon pictures. The Imacon and X-ray pictures taken during the penetration were also used for an extra control of the angle of attack of the projectile.

After the experiments, an axial slice of each backing cylinder, containing a complete crater, was cut out. Then the final penetration in the steel backing was determined from X-ray shadowgraphs.
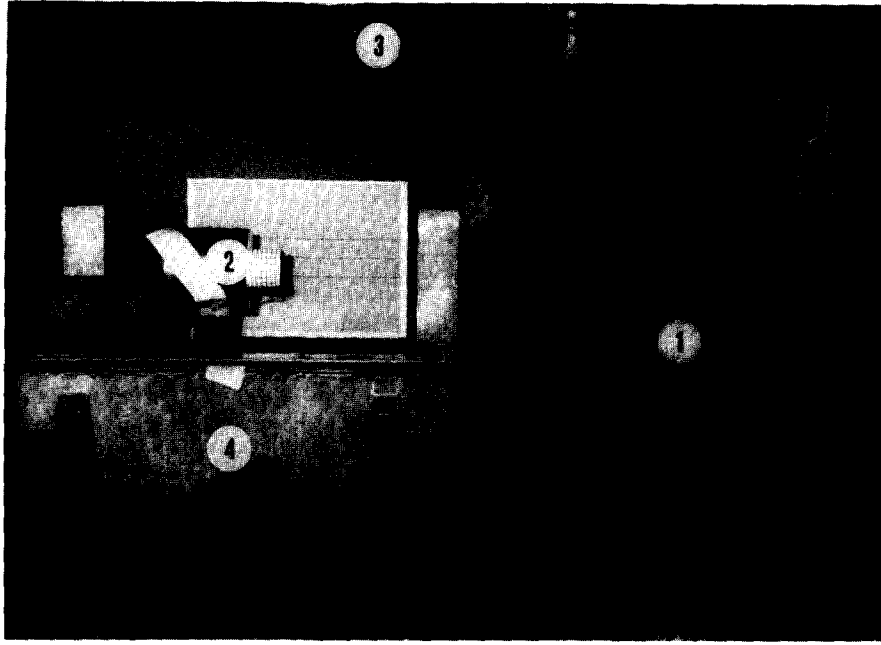
Fig. 3. Experimental set-up seen from the position of the Imacon camera. (1) Sabot catcher, (2) target with background, (3) opening for the 1.2 MV X-ray, and (4) film holder.

SIMULATIONS

AUTODYN [7,8] was used for simulation of the penetration process. This is a coupled (Euler–Lagrange, ALE) finite difference code for transient continuum-dynamical problems. However, the simulations were purely Lagrangian. Also, they were two-dimensional with cylindrical symmetry.

The two geometries shown in Fig. 1 for $1500 \, \text{m s}^{-1}$ and $2500 \, \text{m s}^{-1}$ were studied with the projectile length 75 mm in both cases. The grid for the case of $1500 \, \text{m s}^{-1}$ was set up as follows: the tungsten projectile was divided into 150×5 square zones with size 0.5 mm. The grid in the alumina target consisted of 80 zones in the axial direction and 30 in the radial direction. The zone size was constant in the axial direction but increased as a geometric progression (3.30% per zone) in the radial direction. At the axis of symmetry, the zones were quadratic with size 0.5 mm. In the steel backing the grid consisted of 78 zones axially and 30 zones radially. The zone size increased geometrically in the radial direction (4.64% per zone) and in the axial direction (1.15% per zone) away from the impact interface. The zone at the axis adjacent to the alumina target was quadratic with size 0.8 mm. For the case of $2500 \, \text{m s}^{-1}$, the number of zones in the axial direction in the alumina target was doubled to 160 so that the zone sizes were kept the same as for the case of $1500 \, \text{m s}^{-1}$. In the steel backing the number of zones in the axial direction was increased to 100 in order to keep the zone sizes close to the alumina target and the geometric progression rate (1.16% per zone) the same as for the case of $1500 \, \text{m s}^{-1}$.

For tungsten and steel we used the Johnson–Cook constitutive model [9] which gives the yield limit as

$$\sigma = [A + B(\varepsilon^{\text{p}})^n]\left[1 + C \ln\left(\frac{\dot{\varepsilon}^{\text{p}}}{\dot{\varepsilon}_0}\right)\right]\left[1 - \left(\frac{T - T_0}{T_{\text{m}} - T_0}\right)^m\right], \tag{1}$$

where ε^{p} is the effective plastic strain, $\dot{\varepsilon}^{\text{p}}$ is the plastic strain rate, and T is the temperature. The logarithmic term in Eqn (1) should be set to zero if $\dot{\varepsilon}^{\text{p}}$ is less than the threshold $\dot{\varepsilon}_0$ for strain rate effects. This threshold was taken as $1.0 \, \text{s}^{-1}$. For alumina we used the Johnson–Holmquist constitutive model [5], which is commonly used and easy to implement. We implemented it

by using the AUTODYN user subroutine interface. In Appendix A we have included a brief description of the model and a discussion of the damage growth law. Data for tungsten, steel and alumina used in the simulations are given in Appendix B.

Frictionless boundary conditions were used at interfaces between any combination of the projectile, target and backing materials. Large deformations in the penetration process were handled with the so-called erosion, available in AUTODYN. See [10] for this technique. Zones were considered eroded when the accumulated strain exceeded an erosion strain which is equal to 2.5 for tungsten and steel, and 2.0 for alumina. The erosion strains were set to such high values in order that failure (in the physical sense) should occur before erosion. Too high erosion strains would cause problems due to heavily distorted zones. In [10] values between 1 and 2 are recommended.

DIMENSIONAL CONSIDERATIONS

The geometries of tungsten projectile, alumina target and steel backing, see Fig. 1, are specified by six parameters, viz. the length and diameter of the projectile (L_p, D_p), of the alumina target (L_t, D_t), and of the backing (L_b, D_b). The three materials are characterized by their densities ρ and by parameters that represent their constitutive behaviours and strengths. Thus, there are parameters with dimension of stress such as the Young's moduli E, the shear moduli G, the static yield limits σ, and the hardening moduli H. For tungsten and steel, represented by the Johnson–Cook constitutive model, there is also the threshold strain-rate $\dot{\varepsilon}_0$ for the on-set of strain rate effects, and in addition some dimensionless constants. As mechanical energy is converted into heat by plastic work, the specific heats C_v should also be involved. The fracture toughness K_{Ic} is probably of some importance, especially for alumina, even if it does not appear explicitly in the computational model. These parameters are summarized in Table 1.

Table 1. Parameters characterizing projectile (p), target (t) and backing (b)

Quantity	Unit	Parameter
Lengths	m	L_p, L_t, L_b
Diameters	m	D_p, D_t, D_b
Densities	kgm^{-3}	ρ_p, ρ_t, ρ_b
Young's moduli	Pa	E_p, E_t, E_b
Shear moduli	Pa	G_p, G_t, G_b
Static yield limits	Pa	$\sigma_p, \sigma_t, \sigma_b$
Hardening moduli	Pa	H_p, H_t, H_b
Strain rate thresholds	s^{-1}	$\dot{\varepsilon}_{0p}, \dot{\varepsilon}_{0t}, \dot{\varepsilon}_{0b}$
Fracture toughnesses	$Pam^{1/2}$	$K_{Icp}, K_{Ict}, K_{Icb}$
Specific heats	$Jkg^{-1}K^{-1}$	C_{vp}, C_{vt}, C_{vb}
Impact velocity	ms^{-1}	v_p
Temperatures	K	$T_p = T_t = T_b$

In order to establish dimensionless parameters we normalize all lengths, velocities and densities with respect to those of the projectile (L_p, v_p, ρ_p, respectively). All other reference quantities can be expressed in terms of L_p, v_p, ρ_p and the temperature of the projectile T_p (see Table 2). In [6], dimensional analysis was carried out for a similar problem.

From the experiments we determined the penetration P and the diameter of the alumina target D_t vs time. For penetration, one value was determined from flash radiography in addition to the initial penetration $P_i = 0$ (at time $t = 0$) and the final penetration P_f. Provided that Table 1 contains all the relevant parameters of the problem, the response functions can now be expressed in dimensionless form as

$$\frac{P}{L^*} = f\left(\frac{t}{t^*}, \mathbf{P}\right), \quad \frac{D_t}{L^*} = g\left(\frac{t}{t^*}, \mathbf{P}\right), \tag{2}$$

where

$$\mathbf{P} = \left(\frac{L_t}{L^*}, \frac{L_b}{L^*}, \frac{D_p}{L^*}, \frac{D_t}{L^*}, \frac{D_b}{L^*}, \frac{\rho_t}{\rho^*}, \frac{\rho_b}{\rho^*}, \frac{E_p}{\sigma^*}, \frac{E_t}{\sigma^*}, \frac{E_b}{\sigma^*}, \frac{G_p}{\sigma^*}, \frac{G_t}{\sigma^*}, \frac{G_b}{\sigma^*}, \frac{\sigma_p}{\sigma^*}, \frac{\sigma_t}{\sigma^*}, \frac{\sigma_b}{\sigma^*}, \frac{H_p}{\sigma^*}, \frac{H_t}{\sigma^*}, \frac{H_b}{\sigma^*}, \right.$$

$$\left. \frac{\dot{\varepsilon}_{0p}}{\dot{\varepsilon}^*}, \frac{\dot{\varepsilon}_{0t}}{\dot{\varepsilon}^*}, \frac{\dot{\varepsilon}_{0b}}{\dot{\varepsilon}^*}, \frac{K_{Icp}}{K_I^*}, \frac{K_{Ict}}{K_I^*}, \frac{K_{Icb}}{K_I^*}, \frac{C_{vp}}{C_v^*}, \frac{C_{vt}}{C_v^*}, \frac{C_{vb}}{C_v^*}\right) \tag{3}$$

is a parameter vector. The vector elements consist of the parameters listed in Table 1 (except L_p, ρ_p, v_p, T_p) divided by the corresponding reference quantities from Table 2.

By the scale factor for a quantity X we mean the ratio of the corresponding reference quantity X^* of the model to that of the prototype. Thus, if the scale factor for length is denoted by λ, the replica scale factors will be those shown in Table 2. It follows that every dimensionless element of the parameter vector $\mathbf{P}$ in Eqn (3) will be the same for the model and the prototype except those which involve the strain rate thresholds $\dot{\varepsilon}_0$ and the fracture toughnesses K_{Ic}. Therefore, replica scaling can be expected to be valid only

Table 2. Reference quantities and replica scale factors

Quantity	Unit	Reference quantity (X^*)	Replica scale factor ($X^*_{model}/X^*_{prototype}$)
Length	m	$L^* = L_p$	λ
Velocity	ms^{-1}	$v^* = v_p$	1
Density	kgm^{-3}	$\rho^* = \rho_p$	1
Time	s	$t^* = L_p/v_p$	λ
Stress	Pa	$\sigma^* = \rho_p(v_p)^2$	1
Strain rate	s^{-1}	$\dot{\varepsilon}^* = v_p/L_p$	λ^{-1}
Fracture toughness	Pam$^{1/2}$	$K_I^* = \rho_p(v_p)^2(L_p)^{1/2}$	$\lambda^{1/2}$
Specific heat	Jkg^{-1}K^{-1}	$C_v^* = v_p^2/T_p$	1

if strain rate thresholds and fracture toughnesses have negligible influence on the penetration process.

Next, we will present the experimental results for normalized penetration P/L^* and diameter D_t/L^* vs normalized time t/t^*. Results for different scales are expected to fall on the same curve, if replica scaling is valid. According to our considerations here, deviations from such behaviour would be due to improper scaling of strain rate and fracture toughness (the corresponding dimensionless elements of $\mathbf{P}$ are not the same for the model and the prototype). However, such scale effects could also be caused by other parameters which have been overlooked in Table 1.

RESULTS

Results obtained from the experiments together with corresponding predictions from the computer simulations are shown in Figs 4–8. Figure 4(a) shows an example of a flash X-ray picture of the tungsten projectile during penetration into the alumina target, and Fig. 4(b) shows the corresponding simulated result. From both kinds of results the radial expansion of the alumina target can be observed. For each test, the X-ray picture gives the penetration at one particular time. Such results from eight tests are summarized in Fig. 5.

Figure 6 shows a typical sequence of Imacon pictures from the same test as in Fig. 4(a). The radial expansion vs time for the front end of the alumina targets is plotted in dimensionless form in Fig. 7. In Fig. 8 the normalized final penetration (including the penetration in the steel backing) is plotted versus the length scale represented by the projectile length. The two bars to the right of the diagram represent the alumina target and the steel backing in the same scale as that used in the penetration diagram.

The solid and dashed curves in Figs 5, 7 and 8 represent results of the numerical simulations at $1500\,\mathrm{m\,s^{-1}}$ and $2500\,\mathrm{m\,s^{-1}}$, respectively.

Some data from the tests are given in Table 3.

DISCUSSION

We have investigated the validity of replica scaling which means that the geometrical dimensions are scaled uniformly but velocities and materials are kept the same. For two impact velocities ($1500\,\mathrm{m\,s^{-1}}$, $2500\,\mathrm{m\,s^{-1}}$) the length scale was varied by a factor of five with projectile lengths equal to 30, 75 and 150 mm. The average impact velocities in the two groups of experiments were $1495\,\mathrm{m\,s^{-1}}$ (standard deviation $55\,\mathrm{m\,s^{-1}}$) and $2490\,\mathrm{m\,s^{-1}}$ (standard deviation $40\,\mathrm{m\,s^{-1}}$), respectively. The angle of attack of the rods at impact was generally less than $1.5°$ and never more than $3°$. It was not attempted to compensate the results for the scatter in impact velocity and angle of attack shown in Table 3, besides from using a dimensionless time, the normalization of which depends on impact velocity. One reason is that the scatter in these quantities is relatively unimportant. Another is that we see no unquestionable way to make such a compensation on the basis of two tests only at each scale and nominal impact velocity.

In Fig. 5, the results for P/L^* vs t/t^* from the six tests at $1500\,\mathrm{m\,s^{-1}}$ seem to fall on a single curve, which supports the validity of replica scaling. The numerical simulations show approximately linear dependences of P/L^* on t/t^*, i.e. approximately constant penetration velocities. The experimental points at both $1500\,\mathrm{m\,s^{-1}}$ and $2500\,\mathrm{m\,s^{-1}}$ are slightly above the predicted curves.

The results for D_t/L^* vs t/t^* of the front end of the alumina target in Fig. 7 tend to fall on one curve for $1500\,\mathrm{m\,s^{-1}}$ and on a slightly lower curve for $2500\,\mathrm{m\,s^{-1}}$. These results again support the validity of replica scaling. The agreement with simulation is good at the beginning of the expansion but not at later times. Comparing the diagrams of Figs 5 and 7, we can estimate that the latest points in the latter diagram correspond to times when the projectile should have penetrated well into the backing.

(a)

(b)

Fig. 4. (a) Radiograph 26.15 µs after the impact of a 75 mm projectile on an alumina target at 1490 m s^{-1}. (b) Plot from simulation of the same case with impact velocity at the nominal value 1500 m s^{-1}. The plot is made at 25.98 µs which corresponds to the same dimensionless time as in the radiograph. The shaded areas in the alumina target illustrate the level of damage.

According to the replica scaling laws, the normalized final penetration P_f/L^* for the same velocity should be the same for all length scales L^* in Fig. 8. This seems to hold with fairly good approximation, regardless of the slight scatter in impact velocity and angle of attack. Possibly, there is a slight increase in final penetration depth P_f/L^* with length scale L^* [3]. Linear regression suggests 3.5% and 2.4% increase in P_f/L^* as scale changes by a factor of two at 1500 m s^{-1} and 2500 m s^{-1}, respectively. The computed final penetration agrees well with the measured ones at the lower impact velocity, but the simulation underestimates the final penetration at the higher impact velocity.
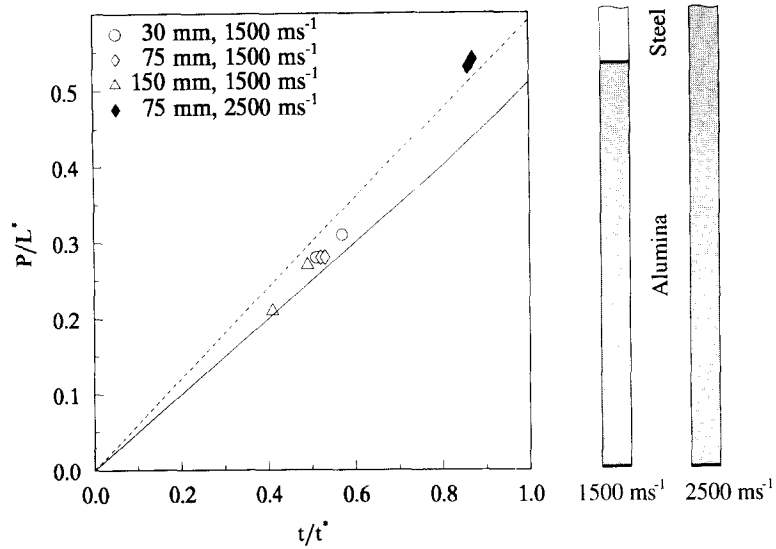
Fig. 5. Measured and computed penetration P/L^* vs time t/t^* for 30, 75 and 150 mm projectiles at $1500\,\mathrm{m\,s^{-1}}$ (open symbols) and for 75 mm projectiles at $2500\,\mathrm{m\,s^{-1}}$ (filled symbols). The computed penetration histories are shown as solid ($1500\,\mathrm{m\,s^{-1}}$) and dashed ($2500\,\mathrm{m\,s^{-1}}$) curves. The alumina (shaded) targets and steel backings are represented by vertical bars.
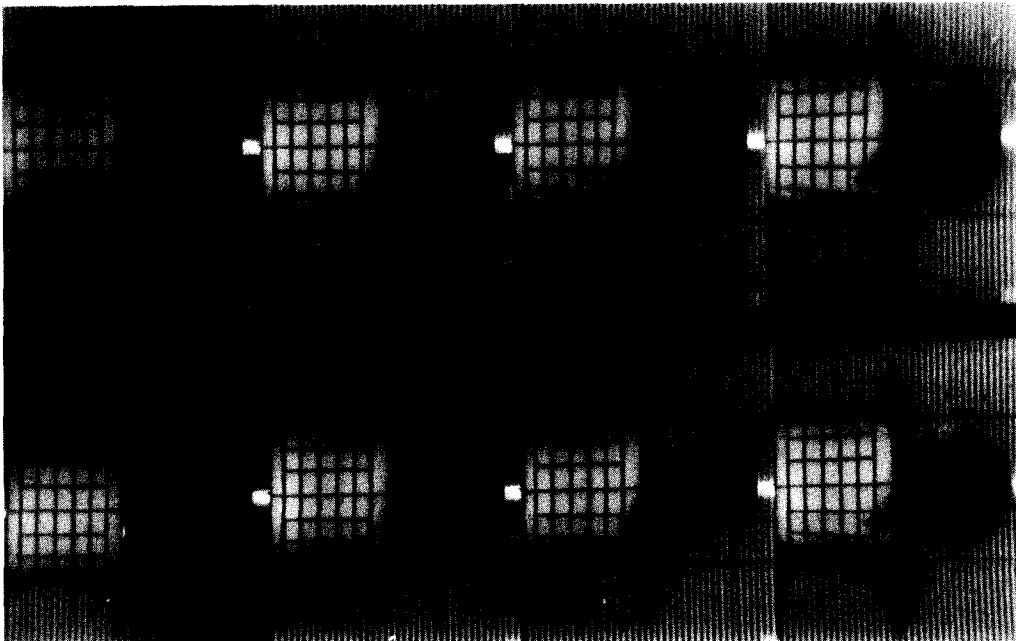

Fig. 6. Imacon pictures of alumina targets from the same test as in Fig. 4(a). The first picture was taken 3.35 μs after impact, and the rest of the pictures with 4.88 μs time interval. The bottom and top rows show pictures 1, 3, 5, 7, and 2, 4, 6, 8, respectively.

As our intention was not to model scale effects, we used a strain-rate independent model for the alumina and performed the simulations for only one geometrical scale. However, the models for the tungsten and steel are strain-rate dependent [9], from which it follows that the computational model is not perfectly invariant under replica scaling. In order to estimate
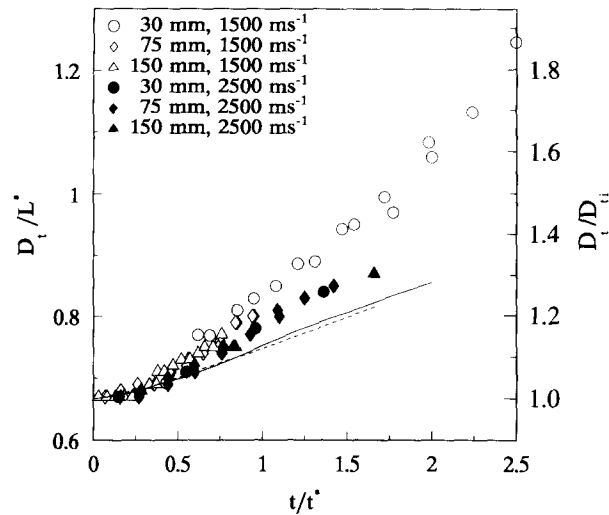
Fig. 7. Measured and computed diameter D_t/L^* (and D_t/D_{ti}, where D_{ti} is the initial diameter) of front end of alumina targets vs time t/t^* for 30, 75 and 150 mm projectiles at 1500 m s^{-1} (open symbols) and 2500 m s^{-1} (filled symbols). The computed diameters are shown as solid (1500 m s^{-1}) and dashed (2500 m s^{-1}) curves.
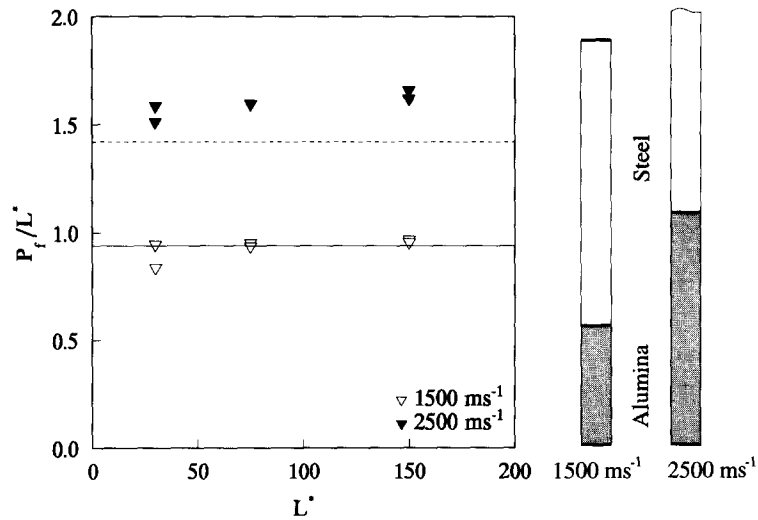

Fig. 8. Measured and computed final penetration depth P_f/L^* vs length scale L^* for 30, 75 and 150 mm projectiles at 1500 m s^{-1} (open symbols) and 2500 m s^{-1} (filled symbols). The computed depths are shown as solid (1500 m s^{-1}) and dashed (2500 m s^{-1}) curves.

the influence of strain-rate, we repeated the simulations with the strain-rate constant $C = 0$ in the Johnson–Cook model. We found that the influence on the normalized penetration, shown in Figs 5 and 8, was less than 0.012, and that the influence on normalized diameter of the alumina target, shown in Fig. 7, was less than 0.04.

We conclude that the laws of replica-scaling hold with sufficient degree of accuracy to justify scaled-down experiments with long tungsten projectiles penetrating unconfined steel-backed alumina targets. Possibly there is a tendency for normalized penetration to increase slightly with scale. Such deviation from replica-scaling could partly be explained by the influences of strain-rate and fracture toughness [6].

Table 3. Data from the tests

Test ID	D_p (mm)	L_p (mm)	v_p (ms^{-1})	Angle of attack (°)	D_t (mm)	L_t (mm)	P_f (mm)
141	2	30	1417	1.7	20	16.1	25.1
142	2	30	1582	2.3	20	15.9	28.3
132	2	30	2409	<1.5	20	32.0	47.6
134	2	30	2475	<1.5	20	32.0	45.4
150	5	75	1488	<1.5	50	40.1	71.4
151	5	75	1503	3.0	50	40.0	70.3
152	5	75	2505	<1.5	50	79.9	119.6
153	5	75	2521	<1.5	50	80.2	119.7
157	10	150	1502	<1.5	100	80.1	145.3
158	10	150	1471	<1.5	100	80.4	143.3
1009	10	150	2505	2.4	100	161.0	249.0
1010	10	150	2485	1.7	100	160.3	243.0

REFERENCES

1. V. Holer and A. J. Stilp, Long rod penetration mechanics. In *High Velocity Impact Dynamics*, pp. 321–382 (Edited by J. A. Zukas). Wiley-Interscience Publication (1990).
2. D. A. Shockey, A. H. Marchand, S. R. Skaggs, G. E. Cort, M. W. Burkett and R. Parker, Failure phenomenology of confined ceramic targets and impacting rods. *Int. J. Impact Engng* 9(3), 263–275 (1990).
3. L. Magness Jr and W. Leonard, Scaling issues for kinetic energy penetrators. *Proc. 14th. Int. Symp. on Ballistics*, Canada, Vol. 2, pp. 281–289 (1993).
4. L. Holmberg, P. Lundberg and L. Westerling, An experimental investigation of WHA long rods penetrating oblique steel plates. *Proc. 14th. Int. Symp. on Ballistics*, Canada, Vol. 2, pp. 515–524 (1993).
5. G. R. Johnson and T. J. Holmquist, An improved computational constitutive model for brittle materials. In *High Pressure Science and Technology*–1993, Vol. 2, pp. 981–984 (Edited by S. C. Schmidt, J. W. Shaner, G. A. Samara and M. Ross). AIP Press, NY (1994).
6. C. E. Anderson, Jr, S. A. Mullin and C. J. Kuhlman, Computer simulation of strain-rate effects in replica scale model penetration experiments. *Int. J. Impact Engng* 13(1), 35–52 (1993).
7. N. K. Birnbaum, M. S. Cowler, M. Itoh, M. Katayama and H. Obata, AUTODYN—an interactive non-linear dynamic analysis program for microcomputers through supercomputers. *9th Int. Conf. on Structural Mechanics in Reactor Technology*, Lausanne, Switzerland August (1987).
8. N. K. Birnbaum and M. S. Cowler, Numerical simulation of impact phenomena in an interactive computing environment. In *Impact Loading and Dynamic Behavior of Materials*, Vol. 2, pp. 881–888 (Edited by C. Y. Chiem, H.-D. Kunze and L. W. Meyer). DGM Informationsgesellschaft mbH, Oberursel (1988).
9. G. R. Johnson and W. H. Cook, A constitutive model and data for metals subjected to large strains, high strain rates, and high temperatures. *Proc. 7th. Int. Symp. on Ballistics*, Holland, pp. 541–547 (1983).
10. G. R. Johnson and R. A. Stryk, Eroding interface and improved tetrahedral element algorithms for high-velocity impact computations in three dimensions. *Int. J. Impact Engng* 5, 411–421 (1987).
11. M. van Thiel, J. Shaner, E. Salinas, T. Michels and C. MacNaughton, Compendium of shock wave data. Lawrence Livermore Laboratory, University of California, Livermore, UCRL-50108, Vol. 1, Sec. A-1, 230–231 (1977).

12. J. Färm and K. G. Sundin, Modified split-Hopkinson pressure bar for testing of high-strength ceramics. *Proc. 10th Int. Conf. on Experimental Mechanics*, Lisbon, Portugal 18–22 July (1994).

13. T. Nicholas and A. M. Rajendran, Mechanical behavior at high strain rates. *Computational Mechanics Associates*, p. 410 (1992).

APPENDIX A: THE JOHNSON–HOLMQUIST MODEL

In the Johnson–Holmquist model [5] the ceramic has a yield stress that decreases with increasing damage. The damage is described by a parameter D which increases gradually from zero to one as the material is damaged. In non-dimensional form the yield stress is given by

$$\sigma' = (1 - D)\sigma'_i + D\sigma'_f, \tag{A1}$$

where σ'_i is the normalized yield stress for the intact material ($D = 0$) and σ'_f is that for the fully damaged material ($D = 1$). The non-dimensional stresses are normalized according to $\sigma' = \sigma/\sigma_{HEL}$, $\sigma'_i = \sigma_i/\sigma_{HEL}$ and $\sigma'_f = \sigma_f/\sigma_{HEL}$ where σ_{HEL} is the effective stress at the Hugoniot Elastic Limit (HEL). The normalized yield stresses for the intact and fully damaged materials depend on the pressure p according to

$$\sigma'_i = A(p' + \sigma'_{hyd})^N, \quad \sigma'_f = B(p')^M. \tag{A2}$$

respectively, where A, B, N, M, and σ'_{hyd} are dimensionless constants. The variable p' is the normalized pressure defined by $p' = p/p_{HEL}$, where p_{HEL} is the hydrostatic pressure at the HEL. The quantity σ_{hyd} is the maximal mean stress which the material can withstand ($\sigma'_{hyd} = \sigma_{hyd}/p_{HEL}$). It is understood that $\sigma'_i = 0$ when $p' < -\sigma'_{hyd}$, and $\sigma_f = 0$ when $p' < 0$. There is also a possibility to limit the yield stress for the fractured material with a dimensionless parameter $S_{f\,max}$ so that $\sigma'_f \leqslant S_{f\,max}$. The Johnson–Holmquist model includes strain rate effects by multiplying the right members of both Eqns (A2) by the factor $(1 + C \ln(\dot{\varepsilon}/\dot{\varepsilon}_0))$, where C and $\dot{\varepsilon}_0$ are constants and $\dot{\varepsilon}$ is the strain rate. In our simulations we do not consider strain rate effects in the ceramic, and therefore the equations have been simplified accordingly.

The increase of the damage parameter D over a time step is proportional to the plastic strain increment $\Delta\varepsilon^p$ with a pressure-dependent proportionality factor. We let the damage accumulate according to

$$D = \Sigma \frac{\Delta\varepsilon^p}{\varepsilon_f^p + \frac{1}{3G}(\sigma_i - \sigma_f)}, \tag{A3}$$

where

$$\varepsilon_f^p = D_1(p' + \sigma'_{hyd})^{D_2}, \tag{A4}$$

and D_1 and D_2 are given constants. The term $(\sigma_i - \sigma_f)/3G$ in the denominator of Eqn (A3) is not present in [5]. It has the effect of reducing the rate of damage growth, and it is derived from the observation that Eqn (A3) is equivalent to the damage evolution law

$$\dot{D} = \frac{\dot{\varepsilon}^p - \dot{\varepsilon}^d}{\varepsilon_f^p}, \tag{A5}$$

where

$$\dot{\varepsilon}^d = -\frac{1}{3G}\frac{\partial\sigma}{\partial D}\dot{D} = \frac{\sigma_i - \sigma_f}{3G}\dot{D} \tag{A6}$$

which can be seen by eliminating $\dot{\varepsilon}^d$ from Eqns (A5) and (A6). In Eqn (A5) the plastic strain which drives the damage evolution is reduced by the plastic strain that is directly caused by the softening due to damage. For our implementation in AUTODYN we obtain better agreement with the test examples in [5] with our modified damage evolution law than with the original one, possibly due to different definitions of plastic strain in the respective codes.

Except for an extra term Δp, which represents the so-called dilatancy, the equation of state is a simple energy-independent pressure–volume relationship

$$p = K_1\mu + K_2\mu^2 + K_3\mu^3 + \Delta p \tag{A7}$$

for $\mu = (\rho/\rho_0) - 1 \geqslant 0$. For $\mu < 0$ the second and third degree terms are omitted, and the pressure is restricted (on the tensile side) to $p \geqslant -(1 - D)\sigma_{hyd}$.

The last term Δp in Eqn (A7) is zero for undamaged material and increases slowly as damage is accumulated. It is determined from an energy consideration. The portion of the decrease of the elastic deviatoric energy which is due only to increase of damage over a time step is

$$\Delta U = \frac{1}{6G}([\sigma(p_{t+\Delta t}, D_t)]^2 - [\sigma(p_{t+\Delta t}, D_{t+\Delta t})]^2), \tag{A8}$$

where $\sigma(p, D)$ is the yield stress as a function of pressure and damage inferred from Eqns (A1) and (A2). Assuming that the fraction β of this energy ΔU is converted to potential hydrostatic energy one can derive [5] the approximate expression

$$\Delta p_{t+\Delta t} = -K_1\mu_{t+\Delta t} + \sqrt{(K_1\mu_{t+\Delta t} + \Delta p_t)^2 + 2\beta K_1 \Delta U} \tag{A9}$$

for the value of Δp at the time $t + \Delta t$.

APPENDIX B: MATERIAL DATA USED IN THE SIMULATIONS

Data for tungsten and steel are listed in Table B1. In [9] data are given for several materials, and we used "tungsten alloy (0.07% Ni, 0.03% Fe)" and "4340 steel". We changed the density for tungsten to a value appropriate for our material (in the reference the density is $17000 \, \text{kgm}^{-3}$). For tungsten we used an equation of state of Mie–Grüneisen type and data for pure tungsten from [11]. The equation of state for steel was a simple energy-independent linear elastic law, based only on a bulk modulus.

For alumina we used the Johnson–Holmquist model with the data listed in Table B2. The elastic moduli K and G are deduced from Poissons ratio, usually reported to be around 0.22, and the measured density, and longitudinal sound speed. Our data are consistent with the longitudinal sound speed $c_l = [(K + (4/3)G)/\rho]^{1/2} = 10.0 \, \text{km s}^{-1}$, Young's modulus $E = 9KG/(3K + G) = 331 \, \text{GPa}$, and Poisson's ratio $v = (3K - 2G)/(6K + 2G) = 0.224$. The compressive strength for the type of alumina used in the experiments has been measured with split Hopkinson pressure bar technique [12] to $\sigma_{\text{comp}} = 3.8 \, \text{GPa}$. For the compressive axial stress at the Hugoniot Elastic Limit we used the value $\text{HEL} = 8.3 \, \text{GPa}$ valid for a similar alumina quality (AD-99.5) [13]. From these values and the tensile strength, which we estimate to be $\sigma_{\text{tens}} = \sigma_{\text{comp}}/10 = 0.38 \, \text{GPa}$, the yield strength curve for the intact material, the first of Eqns (A2), can be determined in the following way. With the assumption that the material responds linearly up to the HEL-point, the three values σ_{HEL}, p_{HEL}, and HEL are proportional to $2G$, K, and $K + (4/3)G$ respectively, i.e. $\sigma_{\text{HEL}}:p_{\text{HEL}}:\text{HEL} = 270:200:380$. Therefore σ_{HEL} and p_{HEL}, used as normalizing quantities in the model, can be determined from $\text{HEL} = 8.3 \, \text{GPa}$ to $\sigma_{\text{HEL}} = (270/380) \, 8.3 = 5.90 \, \text{GPa}$, $p_{\text{HEL}} = (200/380)8.3 = 4.37 \, \text{GPa}$, cf. Table B2. The normalized pressure and yield stress for the intact material satisfy $p' = \sigma_i' = 1$ at HEL. The first of Eqns (A2) then gives

$$A(\sigma_{\text{hyd}}' + 1)^N = 1. \tag{B1}$$

Table B1. Material constants for tungsten and steel used in the simulations

Quantity	Unit	Parameter	Tungsten	Steel
Density	kgm^{-3}	ρ_0	17600	7830
Bulk modulus	GPa	K	–	159
Bulk sound speed	ms^{-1}	c_0	4029	..
Slope in the U_s–U_p–diagram	–	s	1.237	
Grüneisen coefficient	–	Γ	1.54	
Shear modulus	GPa	G	160	81.8
Static yield limit	GPa	A	1.506	0.792
Strain hardening modulus	GPa	B	0.177	0.51
Strain hardening exponent	–	n	0.12	0.26
Coeff. of strain rate	–	C	0.016	0.014
Strain rate threshold	s^{-1}	$\dot{\varepsilon}_0$	1.0	1.0
Thermal softening exponent	–	m	1.0	1.03
Reference temperature	K	T_0	300	300
Specific heat	$\text{Jkg}^{-1}\text{K}^{-1}$	C_v	134	477
Melting temperature	K	T_m	1723	1793

Table B2. Material constants for alumina used in the simulations

Quantity	Unit	Parameter	Alumina
Density	kgm^{-3}	ρ_0	3800
Bulk modulus	GPa	$K = K_1$	200
Coeff. for 2'nd degree term	GPa	K_2	0.0
Coeff. for 3'rd degree term	GPa	K_3	0.0
Shear modulus	GPa	G	135
Effective stress at HEL	GPa	σ_{HEL}	5.9
Pressure at HEL	GPa	P_{HEL}	4.37
Axial stress at HEL	GPa	HEL	8.3
Dimensionless constants:	–	A	0.989
	–	B	0.77
	–	N	0.3755
	–	M	1.0
	–	$S_{f max}$	0.5
	–	σ'_{hyd}	0.029
	–	D_1	0.01
	–	D_2	1.0
	–	β	1.0

In the case of uniaxial stress the mean stress is equal to one third of the axial stress. Therefore σ_{comp} and σ_{tens} (both considered as positive numbers) satisfy

$$\frac{\sigma_{comp}}{\sigma_{HEL}} = A\left(\sigma'_{hyd} + \frac{\sigma_{comp}}{3p_{HEL}}\right)^N \tag{B2}$$

$$\frac{\sigma_{tens}}{\sigma_{HEL}} = A\left(\sigma'_{hyd} - \frac{\sigma_{tens}}{3p_{HEL}}\right)^N. \tag{B3}$$

Because of the steep gradient of the yield strength curve for negative pressures, and the relatively rough estimate of the tensile strength, it is sufficient to set $\sigma'_{hyd} = \sigma_{tens}/(3p_{HEL}) = 0.029$ in order to satisfy Eqn (B3) approximatively. The constants A and N are then determined from Eqns (B1) and (B2), which become linear in logarithmic form.